ACS APPLIED MATERIALS & INTERFACES

www.acsami.org

Research Article

Two-Dimensional MoS_2 Field-Effect Biosensor for Highly Sensitive Detection of Cardiac Troponin I

Yung-Hsin Huang, Yung-Hsuan Chen, Evan Darius, Hui-Fang Shi, Chao-Hui Yeh, Ju-Yin Hsu, and Keng-Ku Liu*

Cite This: *ACS Appl. Mater. Interfaces* 2025, 17, 30740−30746

Read Online

ACCESS | Metrics & More | Article Recommendations | Supporting Information

ABSTRACT: Two-dimensional (2D) materials, particularly transition metal dichalcogenides (TMDs), have gained considerable research attention in electronics and biosensing due to their exceptional electrical and physical properties. In this work, we report a molybdenum disulfide (MoS_2) field-effect-based biosensor for sensitive, selective, and label-free detection of cardiac troponin I (cTnI), a key biomarker for acute myocardial infarction (AMI). To enhance biorecognition efficiency, yolk−shell-structured plasmonic nanoparticles were synthesized and conjugated with anti-cTnI antibodies before being immobilized on the MoS_2 channel surface. The resulting biosensor demonstrated high sensitivity with a limit of detection as low as 2.66 pg/mL. Selectivity tests confirmed its excellent specificity, effectively distinguishing cTnI from other interfering biomarkers. The integration of 2D MoS_2 with yolk−shell nanomaterials provides a highly promising platform for rapid and precise AMI diagnostics.

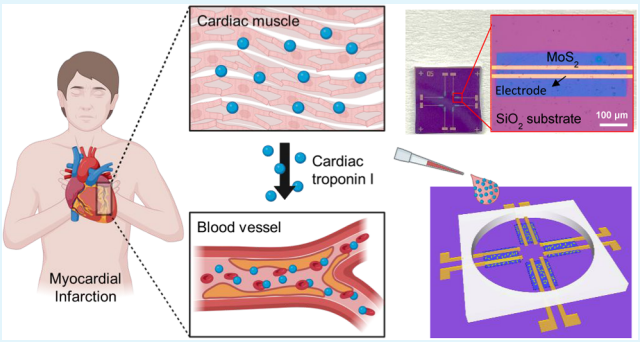

KEYWORDS: *MoS_2, plasmonic nanomaterials, biosensors, cardiovascular disease, cardiac troponin I*

INTRODUCTION

In recent years, cardiovascular disease has emerged as a growing concern within public health systems worldwide.[1] Among its most severe manifestations, acute myocardial infarction (AMI), characterized by the occurrence of myocardial necrosis due to acute obstruction of blood flow and coronary ischemia, is a leading consequence of coronary artery disease.[2] Given that cardiovascular diseases account for nearly one-third of deaths, early and accurate diagnosis is crucial for reducing both morbidity and mortality.[1] Therefore, ultrasensitive and reliable cardiac biomarker quantification is highly essential for effective diagnosis and management.[3] To facilitate early diagnosis of cardiovascular diseases, various cardiac biomarkers are utilized as indicators to evaluate the risk of patients suspected of having acute coronary syndromes who might develop AMI.[4] Cardiac troponin I (cTnI), a biomolecule with molar mass approximately 23.8 kDa, is widely used as a biomarker to detect myocardial damage in patients with AMI due to its significant cardiac specificity.[4,5] As the concentration of cTnI increases within a few hours after the onset of AMI, reaching its maximum level within the next 24 h, it is essential and urgent to reinforce the biosensing platform for timely and precise detection.[1,6,7]

Two-dimensional (2D) materials are at the forefront of materials research due to their exceptional electrical, optical, and electrochemical properties.[8−13] These unique characteristics provide them with unprecedented potential in electronics, biosensing, and energy applications.[14−18] For biosensing applications, there is a growing focus on understanding the interfacing interaction between nanomaterials and biological molecules, which is driving significant advancements in this field.[19−21] Among the various approaches for the fabrication of 2D materials-based biosensors, electrical biosensors have attracted considerable attention for their label-free detection, high sensitivity, rapid response, and portability.[22−24] In particular, atomically layered 2D transition metal dichalcogenides (TMDs), such as molybdenum disulfide (MoS_2), molybdenum diselenide ($MoSe_2$), tungsten disulfide (WS_2), and tungsten diselenide (WSe_2), have been demonstrated to be effective for the next-generation field-effect transistor (FET) biosensors due to their unique electrical and physical properties.[16,21,24,25] On account of their exceptional properties and large surface area, 2D TMDs materials hold significant potential for biosensing applications.

Received: March 25, 2025
Revised: May 1, 2025
Accepted: May 6, 2025
Published: May 16, 2025

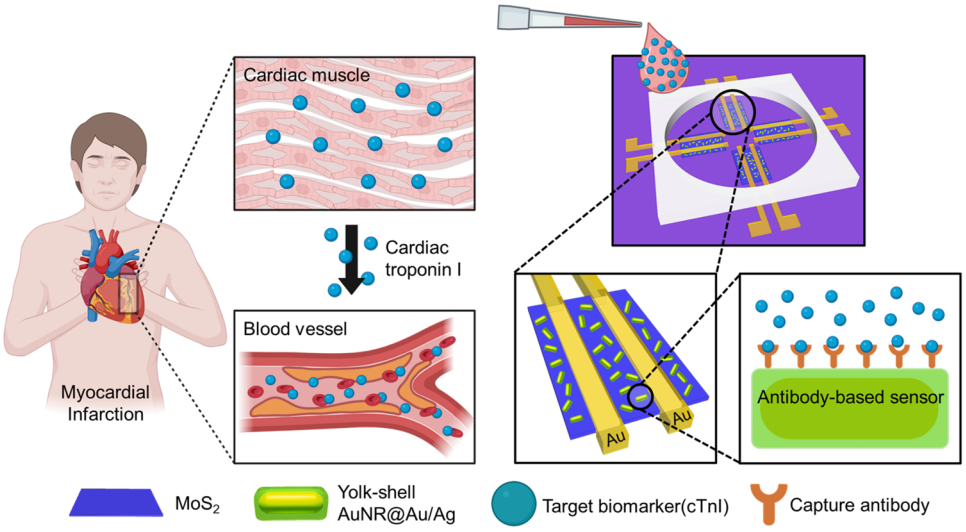

Figure 1. Schematic illustration of the MoS_2 biosensor for cardiac troponin I sensing.

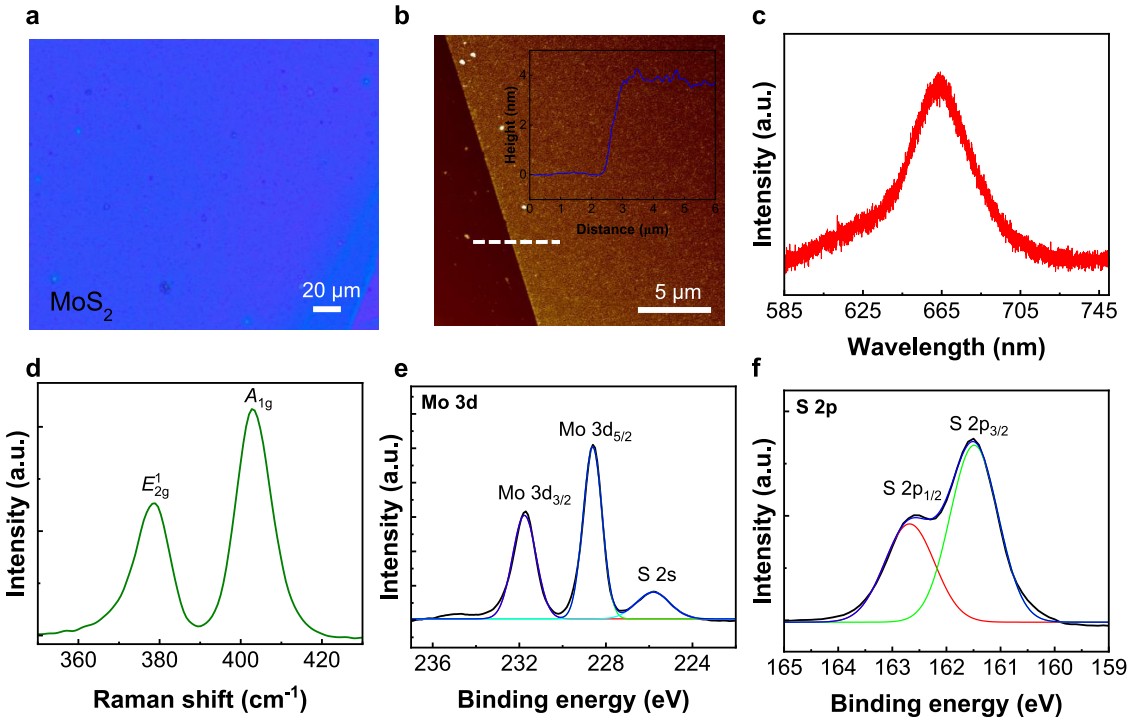

Figure 2. (a) Optical micrograph of the as-synthesized MoS_2. (b) AFM image of the as-synthesized MoS_2. The inset shows the height profile measured along the dashed line. (c) PL spectrum of the as-synthesized MoS_2. (d) Raman spectrum of the as-synthesized MoS_2. (e) XPS spectrum of Mo 3d and S 2s of the as-synthesized MoS_2. (f) XPS spectrum of S 2p of the as-synthesized MoS_2.

In this work, we report MoS_2 field-effect-based biosensors for sensitive and label-free detection of cTnI. Specifically, MoS_2 serves as the channel material in the field-effect biosensor, providing a highly sensitive platform for electrical signal transduction. Meanwhile, yolk−shell-structured plasmonic nanomaterials were synthesized and subsequently conjugated with anti-cTnI antibodies. These antibody-functionalized nanomaterials were immobilized on the MoS_2 channel surface to enhance the surface area of the MoS_2 biosensors and enable the specific detection of target cardiac biomarkers. Utilizing this 2D MoS_2 field-effect biosensing platform, only a small sample volume of 20 μL is required for testing. Our MoS_2 biosensors demonstrated high sensitivity, achieving a limit of detection (LOD) with a concentration as low as 2.66 pg/mL of cTnI. Furthermore, selectivity studies with various interfering proteins confirmed that the MoS_2 biosensors exhibit excellent selectivity for cTnI, meeting the requirements for early AMI diagnosis.

RESULTS AND DISCUSSION

Figure 1 illustrates the integration of yolk−shell plasmonic nanoparticles with MoS_2 as a biosensor for cardiac biomarker sensing. The chemical vapor deposition (CVD) method was used for the growth of 2D MoS_2 nanomaterials (see the Experimental Section). The thickness of the as-synthesized MoS_2 thin layers can be determined using an optical

https://doi.org/10.1021/acsami.5c05963
ACS Appl. Mater. Interfaces 2025, 17, 30740−30746

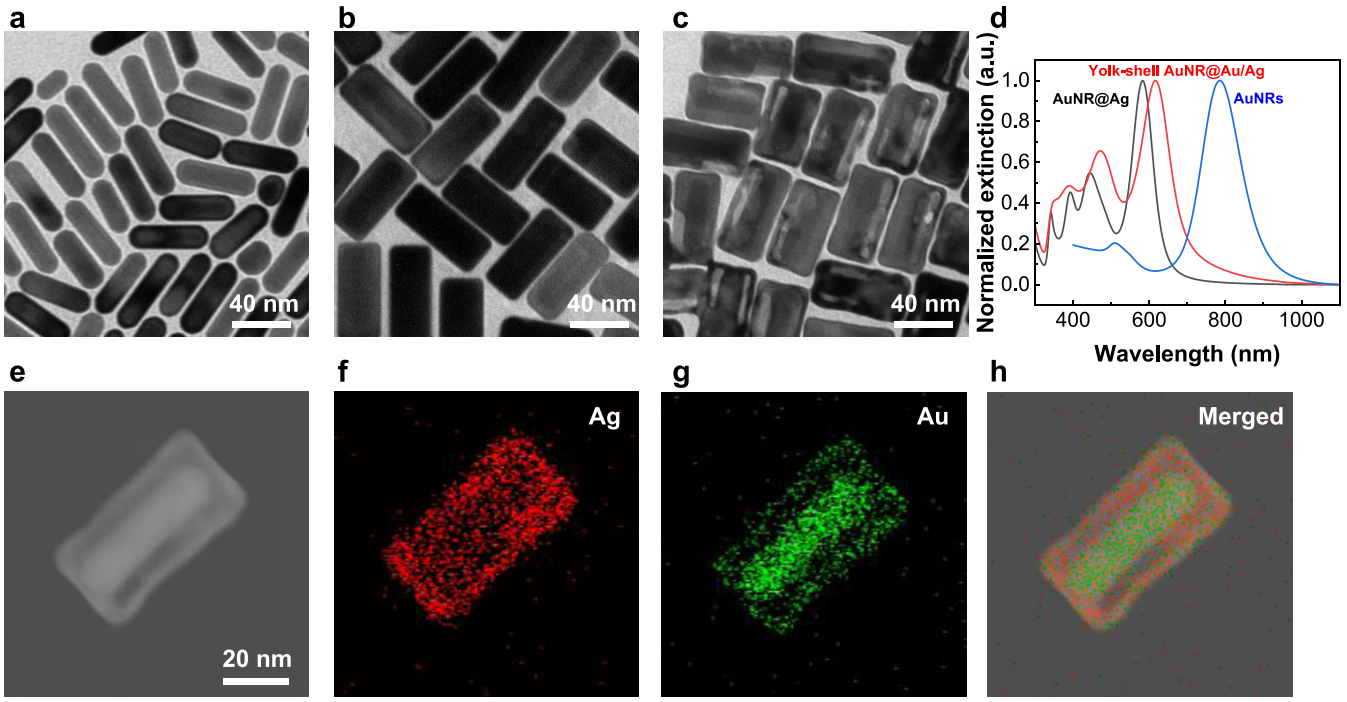

Figure 3. Typical TEM images of (a) AuNRs, (b) AuNR@Ag, and (c) yolk−shell AuNR@Au/Ag. (d) Representative extinction spectra of nanoparticles. (e) HAADF-STEM image and the corresponding EDX elemental mapping of (f) Ag, (g) Au, and (h) merged image of yolk−shell AuNR@Au/Ag.

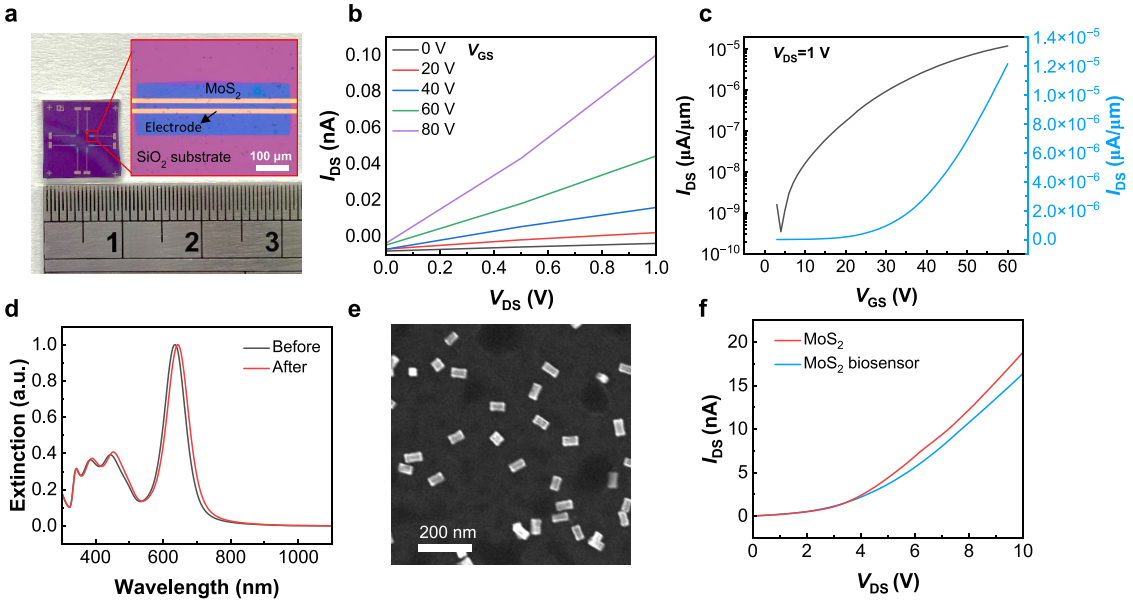

Figure 4. (a) Photograph of the MoS_2 biosensor. The inset shows an optical micrograph of the sensing area in the biosensor. (b) $I_{DS}-V_{DS}$ curves of the MoS_2 FET device with the back-gate voltage varying from 0 to 80 V. (c) $I_{DS}-V_{GS}$ curve and the corresponding logarithmic curve of the MoS_2 FET device. V_{DS} was fixed at 1 V. (d) UV−vis-NIR spectra of yolk−shell AuNR@Au/Ag before and after cTnI-antibody conjugation. (e) Representative SEM image shows the cTnI-antibody-conjugated yolk−shell AuNR@Au/Ag on MoS_2. (f) $I_{DS}-V_{DS}$ curves of the MoS_2 FET device before (red) and after (blue) the adsorption of cTnI-antibody-conjugated yolk−shell AuNR@Au/Ag. V_{GS} is 0 V.

microscope, and the atomic force microscopy (AFM) image revealed a thickness of approximately 3.8 nm (Figures 2a,b). In the photoluminescence (PL) spectrum of MoS_2, a prominent peak can be observed at the wavelength of 663 nm (Figure 2c). Additionally, the Raman spectrum of MoS_2 revealed two characteristic peaks at wavenumbers approximately 379 and 402 cm^{-1}, which correspond to the E^1_{2g} and A_{1g}, respectively (Figure 2d).[26] The as-synthesized MoS_2 was further analyzed via X-ray photoelectron spectroscopy (XPS). The Mo binding energy levels of 228.6 and 231.7 eV correspond to the Mo $3d_{5/2}$ and Mo $3d_{3/2}$, respectively (Figure 2e). A binding energy level of 225.8 eV can be observed with a relatively weak peak intensity, which can be identified as S 2s due to the Mo−S bonding. The binding energies of 161.5 and 162.6 eV can also be observed in the XPS spectrum, which corresponded to the S $2p_{3/2}$ and S $2p_{1/2}$, respectively (Figure 2f).

https://doi.org/10.1021/acsami.5c05963
ACS Appl. Mater. Interfaces 2025, 17, 30740−30746

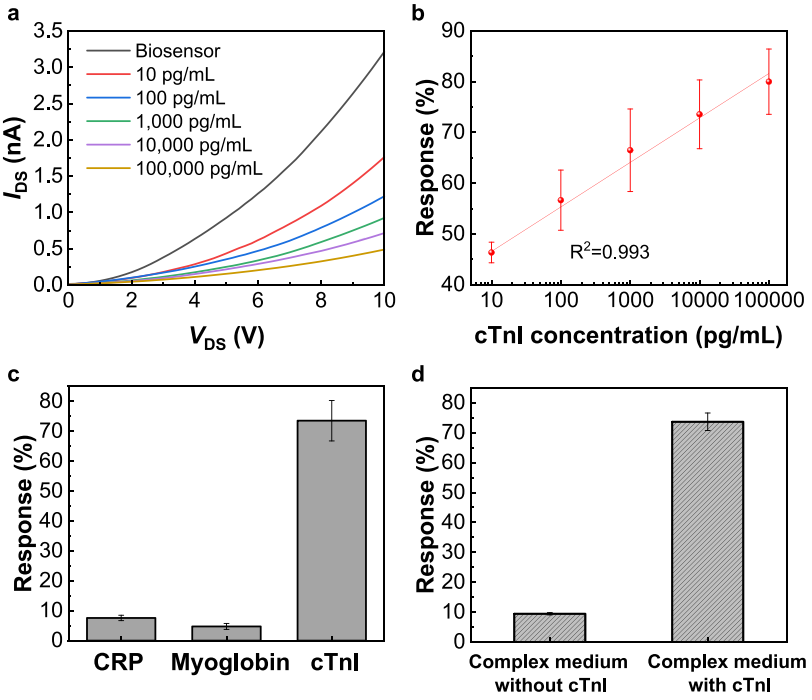

Figure 5. (a) I_{DS}−V_{DS} curves of the MoS_2 biosensor as a function of the cTnI concentration. V_{GS} is 0 V. (b) Response as a function of the cTnI concentration. (c) Response demonstrates its specificity in detecting cTnI compared to two other interfering proteins, CRP and myoglobin. (d) Response of the sensor after exposure to the complex medium without and with cTnI.

After successfully preparing 2D MoS_2, yolk−shell-structured plasmonic nanomaterials were synthesized. A large number of plasmonic nanomaterials on the MoS_2 channel surface will enhance the surface area and increase the available sites for the biorecognition elements on MoS_2 biosensors, ultimately elevating the probe density of the biosensors.[27] These high-density probes will be beneficial for sensitively detecting specific cardiac biomarkers. A two-step procedure was employed for the synthesis of yolk−shell nanoparticles.[28,29] The procedure started with the growth of gold nanorods (AuNRs), which served as the cores of the yolk−shell-structured plasmonic nanoparticles (see Supporting Information for details). The size and shape of the as-synthesized AuNRs can be observed using a transmission electron microscope (TEM), and the edge length and width were measured to be 52.2 ± 4.0 and 16.4 ± 1.7 nm, respectively (Figures 3a and S1). The aqueous solution of silver nitrate ($AgNO_3$) was added as a precursor of silver, using ascorbic acid as the reducing agent and hexadecyltrimethylammonium chloride (CTAC) as the capping agent, into the AuNRs suspension. A uniform thin layer of Ag was deposited on the surface of AuNRs, forming AuNR core-Ag shell (AuNR@Ag) nanomaterials (Figure 3b). Their average length and width determined from the TEM image were 64.1 ± 4.0 and 28.2 ± 1.7 nm, respectively (Figure S2). A galvanic replacement reaction was employed to transform the solid structure of AuNR@Ag into porous and yolk−shell-structured plasmonic nanomaterials. An aqueous $HAuCl_4$ solution was put in the AuNR@Ag suspension, resulting in the yolk−shell-structured plasmonic nanoparticles (Figure 3c). The average dimensions were also determined from the TEM image, which displayed a length of 63.2 ± 3.6 nm and a width of 32.7 ± 1.6 nm (Figure S3). Ultraviolet (UV)−vis-NIR spectra of AuNRs, AuNR@Ag, and yolk−shell AuNR@Au/Ag were collected (Figure 3d). The longitudinal and transverse plasmon resonance wavelengths of the AuNRs dispersed in aqueous solutions are 785 and 510 nm, respectively. Four plasmon resonance bands can be observed at wavelengths of 341, 392, 444, and 582 nm in the spectrum of AuNR@Ag. In addition, the UV−vis-NIR spectrum of yolk−shell AuNR@Au/Ag shows four plasmon resonance bands at wavelengths of 348, 389, 471, and 616 nm. The energy-dispersive X-ray spectroscopy (EDX) elemental mapping results revealed the bimetallic composition of gold and silver within the yolk−shell AuNR@Au/Ag (Figure 3e-h).

Following the synthesis and characterization of nanomaterials as building blocks for biosensors, we moved forward with the fabrication of 2D MoS_2 biosensors. The channel length of these biosensors was designed to be 20 μm, and we utilized a standard lithography-based manufacturing process for their construction. A total of eight biosensors were arranged on a biosensing chip with a size of 1 × 1 cm^2, and the sensing area in the biosensor was close to the center area of the biosensing chip (Figure 4a). The output characteristics (I_{DS}−V_{DS} curves) of the n-type MoS_2 device are shown in Figure 4b. The transfer characteristics (I_{DS}-V_{GS} curves) of the MoS_2 device in logarithmic (black curve) and linear (blue curve) scales were measured at a drain voltage of 1 V (Figure 4c). The on/off ratio of the n-type MoS_2 device was calculated to be 3.46 × 10^4. After successful preparation of the MoS_2 device, we proceeded with the surface functionalization of the MoS_2 device. The cTnI antibodies were conjugated onto yolk−shell AuNR@Au/Ag via the 1-(3-(dimethylamino)propyl)-3-ethylcarbodiimide hydrochloride (EDC)/*N*-hydroxysuccinimide (NHS) method (see the details in the Experimental Section). After the conjugation of cTnI antibodies, a red shift of 9 nm was observed in the LSPR spectrum (Figure 4d and Figure S4). Next, cTnI antibody-modified yolk−shell AuNR@Au/Ag nanostructures were adsorbed on the 2D MoS_2 channel surface via electrostatic interaction using poly(sodium-4-styrenesulfonate) (PSS) (Figure 4e, please see Experimental

https://doi.org/10.1021/acsami.5c05963
ACS Appl. Mater. Interfaces 2025, 17, 30740−30746

Section and Supporting Information for the detailed procedure). The output characteristics of the MoS_2 device were measured before (red) and after (blue) the adsorption of these nanostructures (Figure 4f). From the output characteristics, the drain current was observed to be decreased after the adsorption of cTnI antibody-modified yolk−shell AuNR@Au/Ag nanostructures. This decrease in current may be attributed to the charge transfer and accumulation effect induced by the cTnI antibody-modified yolk−shell AuNR@Au/Ag nanostructures.[27] The MoS_2 biosensor, prepared with the adsorption of cTnI antibody-modified yolk−shell AuNR@Au/Ag nanostructures on the channel surface of the MoS_2 device, is ready for detection of the target biomarker cTnI.

To access the sensing performance of the MoS_2 biosensor, we tested a 1× Tris-buffered saline (TBS) solution (pH 7.4) spiked with cTnI at various concentrations ranging from 0 to 100,000 pg/mL. Figure 5a shows the $I_{DS}-V_{DS}$ curves of the MoS_2 biosensor as a function of the cTnI concentration. As the cTnI protein concentration increases, a significant decrease in the current is observed. This behavior is due to the molecular gating effect of the negatively charged cTnI protein, i.e., p-doping, which decreased the electron carrier concentration in MoS_2.[22,27] During the sensing experiments, the sensing response is employed to evaluate the sensitivity of the MoS_2 biosensor, which is defined as $((I_0 - I_f)/I_0) \times 100\%$, where I_0 and I_f represent the currents in the $I_{DS}-V_{DS}$ curves before and after cTnI detection, respectively. As shown in Figure 5b, the MoS_2 biosensor can detect a cTnI concentration as low as 10 pg/mL, which is below the typical cTnI levels found in human blood.[7,30] The calibration curve indicates a strong correlation between the concentration of cTnI and the response of the MoS_2 biosensor, with a coefficient of determination (R^2) of 0.993. Additionally, notable differences in response were observed after incubation in 1× TBS containing cTnI at concentrations of 0 and 10 pg/mL, indicating the exceptional sensitivity of the MoS_2 biosensor for detecting low concentrations of target biomarkers (Figure S5). The LOD was calculated to be 2.66 pg/mL (average signal obtained from the blank sample plus three times its standard deviation). Furthermore, we performed experiments to compare the binding capacities of our biosensors (i.e., anti-cTnI/yolk−shell AuNR@Au/Ag/MoS_2) with those fabricated via direct antibody immobilization (i.e., anti-cTnI/MoS_2). For the preparation of directly immobilized biosensors, anti-cTnI antibodies were immobilized onto MoS_2 using a thiol-based functionalization method. The anti-cTnI/MoS_2 biosensors were then exposed to 1× TBS containing cTnI at a concentration of 10 pg/mL. Compared to the response observed from the anti-cTnI/yolk−shell AuNR@AuAg/MoS_2 biosensor under identical conditions (exposure to cTnI at a concentration of 10 pg/mL), the signal obtained from the directly immobilized anti-cTnI/MoS_2 biosensors was significantly lower (Figure S6 in the Supporting Information). These results clearly demonstrate that yolk−shell AuNR@Au/Ag substantially enhances the sensing performance of the MoS_2 biosensor. To verify the specificity, the MoS_2 biosensors were tested with two nontarget biomarkers, C-reactive protein (CRP, 10 ng/mL) and myoglobin (250 ng/mL). As shown in Figure 5c, the response of the biosensor to cTnI (73.55 ± 6.8%) was significantly higher than its responses to CRP (7.58 ± 0.9%) and myoglobin (4.74 ± 1.0%). Furthermore, the selectivity of the biosensors was evaluated in complex media with and without cTnI. The complex medium was composed of various biomolecules found in the human body within normal levels, including hemoglobin (15 g/dL), albumin (4 g/dL), glucose (75 mg/dL), uric acid (5 mg/dL), CRP (10 ng/mL), and myoglobin (250 ng/mL) in 1× TBS. When exposed to the complex medium without cTnI, the biosensor showed a response of approximately 9.45 ± 0.4% (Figure 5d). In contrast, in the presence of cTnI (10 ng/mL), the response increased significantly to 73.65 ± 2.9%, demonstrating the remarkable specificity of the MoS_2 biosensors.

CONCLUSIONS

In summary, we have successfully developed a highly sensitive and selective 2D MoS_2 field-effect biosensing platform for the label-free detection of cTnI, which is a crucial biomarker for acute myocardial infarction. By integrating yolk−shell-structured plasmonic nanomaterials with MoS_2, the surface area and biorecognition efficiency were significantly enhanced, achieving a remarkable LOD as low as 2.66 pg/mL. The biosensor demonstrated a strong correlation between cTnI concentration and response, with a high coefficient of determination (R^2 = 0.993). Furthermore, specificity studies confirmed minimal cross-reactivity with nontarget biomarkers, reinforcing the suitability of the biosensor for early and precise AMI diagnosis.

EXPERIMENTAL SECTION

Chemical Vapor Deposition of MoS_2. Two-dimensional MoS_2 was synthesized by using the chemical vapor deposition method. First, the MoO_3 powder (around 3 mg) was placed in a quartz boat in the center of the furnace. The S powder (0.5 g) was placed in a separate quartz boat in the upper stream of the furnace. The SiO_2/Si substrate was cleaned using a piranha solution, followed by a sonication process in nanopure water for 10 min. The clean SiO_2/Si substrate was placed face down above the quartz boat containing MoO_3 powder. The gas flow (80 sccm of Ar) was introduced into the chamber, and the pressure was controlled at 50 Torr. The center zone of the furnace was heated to 750 °C and kept there for 10 min.

Yolk−Shell AuNR@Au/Ag-cTnI Antibody Conjugate. Yolk−shell AuNR@Au/Ag-cTnI antibody conjugate was obtained using an EDC/NHS method.[31,32] Please see the Supporting Information for the detailed procedure.

Adsorption of Nanoparticle-cTnI Antibody Conjugate on MoS_2. Please see the Supporting Information for the detailed procedure.

Biosensing Test. During the sensing experiments, cTnI protein was spiked in a 1× TBS solution (pH 7.4), and 20 μL of the sample was incubated in the sensing area of the MoS_2 biosensor for 1h. After incubation, the biosensor was rinsed with 1× TBS and nanopure water and then dried using nitrogen gas. The electrical experiments were conducted with a Keysight B1500A and Keithley 4200 analyzers. The sensor response is defined as $((I_0 - I_f)/I_0) \times 100\%$, where I_0 and I_f represent the currents in the $I_{DS}-V_{DS}$ curves before and after cTnI detection, respectively, at a source-drain voltage (V_{DS}) of 8 V.

Characterization Techniques. UV−vis-NIR experiments were performed with a Shimadzu UV-1900 spectrophotometer. SEM experiments were conducted with a JEOL JSM-7610F instrument. TEM images were collected with a JEOL JEM-2100 instrument. EDX spectroscopy is affiliated with the TEM instrument. AFM experiments were conducted with a Bruker Dimension ICON. XPS experiments were conducted with a high-resolution electron spectrometer (ULVAC-PHI). Raman and PL spectra were obtained by using a Horiba iHR-550 Raman spectrometer with a 532 nm laser.

ASSOCIATED CONTENT

Supporting Information

The Supporting Information is available free of charge at https://pubs.acs.org/doi/10.1021/acsami.5c05963.

https://doi.org/10.1021/acsami.5c05963
ACS Appl. Mater. Interfaces 2025, 17, 30740−30746

Materials; synthesis of plasmonic nanomaterials; size distribution of plasmonic nanomaterials; functionalization of cTnI antibodies, and response of the MoS_2 biosensor (PDF)

AUTHOR INFORMATION

Corresponding Author

Keng-Ku Liu − *Department of Biomedical Engineering and Environmental Sciences, National Tsing Hua University, Hsinchu 300044, Taiwan;* orcid.org/0000-0002-1427-3494; Email: kkliu@mx.nthu.edu.tw

Authors

Yung-Hsin Huang − *Department of Biomedical Engineering and Environmental Sciences, National Tsing Hua University, Hsinchu 300044, Taiwan*

Yung-Hsuan Chen − *Department of Biomedical Engineering and Environmental Sciences, National Tsing Hua University, Hsinchu 300044, Taiwan*

Evan Darius − *Department of Biomedical Engineering and Environmental Sciences, National Tsing Hua University, Hsinchu 300044, Taiwan*

Hui-Fang Shi − *Department of Biomedical Engineering and Environmental Sciences, National Tsing Hua University, Hsinchu 300044, Taiwan*

Chao-Hui Yeh − *Department of Electrical Engineering, Institute of Electronics Engineering, Center for Nanotechnology, Materials Science and Microsystem, and College of Semiconductor Research, National Tsing Hua University, Hsinchu 300044, Taiwan;* orcid.org/0000-0002-9437-055X

Ju-Yin Hsu − *National Taiwan University Hospital Hsinchu Branch, Hsinchu 300001, Taiwan*

Complete contact information is available at: https://pubs.acs.org/10.1021/acsami.5c05963

Author Contributions

K.K.L. designed the research. Y.H.H., Y.H.C., E.D., H.F.S., C.H.Y., J.Y.H., and K.K.L. performed, analyzed, and supervised the experiments. K.K.L. wrote the manuscript. All authors read and commented on the manuscript.

Notes

The authors declare no competing financial interest.

ACKNOWLEDGMENTS

This work was supported by grants from the NSTC (112−2221−E−007−096 and 113-2221-E-007−023), NTHU (113QF033E1), the Instrumentation Center (113−2740−M−007−001) at NTHU, and NTU Hospital Hsinchu Branch (113−HCH110). The authors thank Prof. Ching-Yuan Su at National Central University for providing access to the semiconductor device analyzer and Raman spectrometer. The schematic and TOC graphic were created by Y.-H.H. using Biorender and Blender.

REFERENCES

(1) Joseph, P.; Yusuf, S. Coordinating Efforts to Reduce the Global Incidence of Cardiovascular Disease. *N. Engl. J. Med.* **2023**, *389*, 1329−1331.

(2) Anderson, J. L.; David, A. M. Acute Myocardial Infarction. *N. Engl. J. Med.* **2017**, *376*, 2053−2064.

(3) Lim, W. Y.; Goh, C.-H.; Thevarajah, T. M.; Goh, B. T.; Khor, S. M. Using SERS-based microfluidic paper-based device (μPAD) for calibration-free quantitative measurement of AMI cardiac biomarkers. *Biosens. Bioelectron.* **2020**, *147*, No. 111792.

(4) Hachey, B. J.; Kontos, M. C.; Newby, L. K.; Christenson, R. H.; Peacock, W. F.; Brewer, K. C.; McCord, J. Trends in Use of Biomarker Protocols for the Evaluation of Possible Myocardial Infarction. *J. Am. Heart Assoc.* **2017**, *6*, No. e005852.

(5) Schmid, J.; Liesinger, L.; Birner-Gruenberger, R.; Stojakovic, T.; Scharnagl, H.; Dieplinger, B.; Asslaber, M.; Radl, R.; Beer, M.; Polacin, M.; Mair, J.; Szolar, D.; Berghold, A.; Quasthoff, S.; Josepha, S. B.; Peter, P. R. Elevated Cardiac Troponin T in Patients With Skeletal Myopathies. *J. Am. Coll. Cardiol.* **2018**, *71*, 1540−1549.

(6) Spain, E.; Carrara, S.; Adamson, K.; Ma, H.; O'Kennedy, R.; De Cola, L.; Forster, R. J. Cardiac Troponin I: Ultrasensitive Detection Using Faradaic Electrochemical Impedance. *ACS Omega* **2018**, *3*, 17116−17124.

(7) Yola, M. L.; Atar, N. Development of cardiac troponin-I biosensor based on boron nitride quantum dots including molecularly imprinted polymer. *Biosens. Bioelectron.* **2019**, *126*, 418−424.

(8) Shi, Y.; Li, H.; Li, L.-J. Recent advances in controlled synthesis of two-dimensional transition metal dichalcogenides via vapour deposition techniques. *Chem. Soc. Rev.* **2015**, *44*, 2744−2756.

(9) Cai, X.; Luo, Y.; Liu, B.; Cheng, H.-M. Preparation of 2D material dispersions and their applications. *Chem. Soc. Rev.* **2018**, *47*, 6224−6266.

(10) Li, H.; Li, Y.; Aljarb, A.; Shi, Y.; Li, L.-J. Epitaxial Growth of Two-Dimensional Layered Transition-Metal Dichalcogenides: Growth Mechanism, Controllability, and Scalability. *Chem. Rev.* **2018**, *118*, 6134−6150.

(11) Pham, P. V.; Bodepudi, S. C.; Shehzad, K.; Liu, Y.; Xu, Y.; Yu, B.; Duan, X. 2D Heterostructures for Ubiquitous Electronics and Optoelectronics: Principles, Opportunities, and Challenges. *Chem. Rev.* **2022**, *122*, 6514−6613.

(12) Wu, R.; Zhang, H.; Ma, H.; Zhao, B.; Li, W.; Chen, Y.; Liu, J.; Liang, J.; Qin, Q.; Qi, W.; Chen, L.; Li, J.; Li, B.; Duan, X. Synthesis, Modulation, and Application of Two-Dimensional TMD Heterostructures. *Chem. Rev.* **2024**, *124*, 10112−10191.

(13) Liu, J.; Smith, S.; Wang, C. Photothermal Attenuation of Cancer Cell Stemness, Chemoresistance, and Migration Using CD44-Targeted MoS2 Nanosheets. *Nano Lett.* **2023**, *23*, 1989−1999.

(14) Akinwande, D.; Huyghebaert, C.; Wang, C.-H.; Serna, M. I.; Goossens, S.; Li, L.-J.; Wong, H. S. P.; Koppens, F. H. L. Graphene and two-dimensional materials for silicon technology. *Nature* **2019**, *573*, 507−518.

(15) Das, S.; Sebastian, A.; Pop, E.; McClellan, C. J.; Franklin, A. D.; Grasser, T.; Knobloch, T.; Illarionov, Y.; Penumatcha, A. V.; Appenzeller, J.; Chen, Z.; Zhu, W.; Asselberghs, I.; Li, L.-J.; Avci, U. E.; Bhat, N.; Anthopoulos, T. D.; Singh, R. Transistors based on two-dimensional materials for future integrated circuits. *Nat. Electron.* **2021**, *4*, 786−799.

(16) Rohaizad, N.; Mayorga-Martinez, C. C.; Fojtů, M.; Latiff, N. M.; Pumera, M. Two-dimensional materials in biomedical, biosensing and sensing applications. *Chem. Soc. Rev.* **2021**, *50*, 619−657.

(17) Bonaccorso, F.; Colombo, L.; Yu, G.; Stoller, M.; Tozzini, V.; Ferrari, A. C.; Ruoff, R. S.; Pellegrini, V. Graphene, related two-dimensional crystals, and hybrid systems for energy conversion and storage. *Science* **2015**, *347*, No. 1246501.

(18) Siao, M.-D.; Tsai, M.-Y.; Gandhi, A. C.; Wu, Y.-C.; Fan, T.; Hao, L.-S.; Li, I. L.; Chen, S.-Z.; Liu, C.-H.; Lin, Y.-F.; Yeh, C.-H. Two-Dimensional Phototransistors with van der Waals Superstructure Contacts for High-Performance Photosensing. *ACS Appl. Mater. Interfaces* **2025**, *17*, 6521−6529.

(19) Lin, C.-T.; Loan, P. T. K.; Chen, T.-Y.; Liu, K.-K.; Chen, C.-H.; Wei, K.-H.; Li, L.-J. Label-Free Electrical Detection of DNA Hybridization on Graphene using Hall Effect Measurements: Revisiting the Sensing Mechanism. *Adv. Funct. Mater.* **2013**, *23*, 2301−2307.

(20) Park, H.; Baek, S.; Sen, A.; Jung, B.; Shim, J.; Park, Y. C.; Lee, L. P.; Kim, Y. J.; Kim, S. Ultrasensitive and Selective Field-Effect

Transistor-Based Biosensor Created by Rings of MoS2 Nanopores. *ACS Nano* **2022**, *16*, 1826−1835.
(21) De Silva, T.; Fawzy, M.; Hasani, A.; Ghanbari, H.; Abnavi, A.; Askar, A.; Ling, Y.; Mohammadzadeh, M. R.; Kabir, F.; Ahmadi, R.; Rosin, M.; Kavanagh, K. L.; Adachi, M. M. Ultrasensitive rapid cytokine sensors based on asymmetric geometry two-dimensional MoS2 diodes. *Nat. Commun.* **2022**, *13*, No. 7593.
(22) Sarkar, D.; Liu, W.; Xie, X.; Anselmo, A. C.; Mitragotri, S.; Banerjee, K. MoS2 Field-Effect Transistor for Next-Generation Label-Free Biosensors. *ACS Nano* **2014**, *8*, 3992−4003.
(23) Luo, X.; Davis, J. J. Electrical biosensors and the label free detection of protein disease biomarkers. *Chem. Soc. Rev.* **2013**, *42*, 5944−5962.
(24) Fathi-Hafshejani, P.; Azam, N.; Wang, L.; Kuroda, M. A.; Hamilton, M. C.; Hasim, S.; Mahjouri-Samani, M. Two-Dimensional-Material-Based Field-Effect Transistor Biosensor for Detecting COVID-19 Virus (SARS-CoV-2). *ACS Nano* **2021**, *15*, 11461−11469.
(25) Dai, C.; Liu, Y.; Wei, D. Two-Dimensional Field-Effect Transistor Sensors: The Road toward Commercialization. *Chem. Rev.* **2022**, *122*, 10319−10392.
(26) Liu, K.-K.; Zhang, W.; Lee, Y.-H.; Lin, Y.-C.; Chang, M.-T.; Su, C.-Y.; Chang, C.-S.; Li, H.; Shi, Y.; Zhang, H.; Lai, C.-S.; Li, L.-J. Growth of Large-Area and Highly Crystalline MoS2 Thin Layers on Insulating Substrates. *Nano Lett.* **2012**, *12*, 1538−1544.
(27) Liu, J.; Chen, X.; Wang, Q.; Xiao, M.; Zhong, D.; Sun, W.; Zhang, G.; Zhang, Z. Ultrasensitive Monolayer MoS2 Field-Effect Transistor Based DNA Sensors for Screening of Down Syndrome. *Nano Lett.* **2019**, *19*, 1437−1444.
(28) Hsu, Y.-T.; Lin, S.-H.; Liu, K.-K. A flexible plasmonic substrate for sensitive surface-enhanced Raman scattering-based detection of fentanyl. *Chem. Commun.* **2024**, *60*, 13903−13906.
(29) Hsu, Y.-T.; Chen, C.-H.; Hsu, J.-Y.; Chen, H.-W.; Liu, K.-K. Femtosecond laser-induced Au nanostructure-decorated with plasmonic nanomaterials for sensitive SERS-based detection of fentanyl. *Talanta* **2025**, *284*, No. 127264.
(30) Tadepalli, S.; Kuang, Z.; Jiang, Q.; Liu, K.-K.; Fisher, M. A.; Morrissey, J. J.; Kharasch, E. D.; Slocik, J. M.; Naik, R. R.; Singamaneni, S. Peptide Functionalized Gold Nanorods for the Sensitive Detection of a Cardiac Biomarker Using Plasmonic Paper Devices. *Sci. Rep.* **2015**, *5*, No. 16206.
(31) Lu, Y.-C.; Darius, E.; Lien, M.-C.; Yeh, I. H.; Shi, H.-F.; Huang, Y.-H.; Chen, C.-H.; Chen, H.-W.; Su, C.-Y.; Hsu, R.-Y.; Liu, K.-K. Two-Dimensional Cs2AgBiBr6-Based Biosensor for Selective and Sensitive Detection of Cardiac Biomarker Troponin I. *ACS Appl. Nano Mater.* **2023**, *6*, 23022−23028.
(32) Yeh, I. H.; Shi, H.-F.; Darius, E.; Lien, M.-C.; Lu, Y.-C.; Wang, C.; Liu, K.-K. Plasmonic biochips with enhanced stability in harsh environments for the sensitive detection of prostate-specific antigen. *J. Mater. Chem. B* **2024**, *12*, 1617−1623.

https://doi.org/10.1021/acsami.5c05963
ACS Appl. Mater. Interfaces 2025, 17, 30740−30746